



Supplementary Materials for

The Complete Structure of the 55S Mammalian Mitochondrial Ribosome

Basil J. Greber^{*}, Philipp Bieri^{*}, Marc Leibundgut^{*}, Alexander Leitner, Ruedi Aebersold,
Daniel Boehringer, Nenad Ban

correspondence to: ban@mol.biol.ethz.ch
^{*}these authors contributed equally to this work

This PDF file includes:

Materials and Methods
Supplementary Text
Figs. S1 to S10
Tables S1 to S7
References (41-67)

Other Supplementary Materials for this manuscript includes the following:

Additional Data Table S1

Materials and Methods

Sample preparation, data acquisition, and initial data processing

The determination of the porcine 28S subunit structure was based on the cryo-EM particle dataset that was previously used for determination of the structure of the 39S subunit. Sample preparation, data acquisition, and initial data processing are described in detail in ref. (14). In brief, mitoribosomes were isolated from porcine mitochondria prepared from liver tissue, applied to Quantifoil R2/2 cryo-EM grids on a continuous carbon film, flash frozen, and imaged in a FEI Titan Krios cryo-electron microscope (FEI Company). Images were acquired and fractionated into seven sub-frames on a FEI Falcon II (FEI Company) direct electron detector using the EPU software (FEI Company). Sub-frame alignment was performed using DOSEFGPU DRIFTCORR (41), with each micrograph divided into four sections for which drift was assessed and corrected individually. Particle selection and initial image processing were performed using Batchboxer (42) and CTFFIND (43) as described (14), and particle images were subjected to initial 2D- and 3D-classification to isolate a population of 141'700 particle images (14).

Image processing for determination of 28S subunit structure

The magnification was re-calibrated for the present study to be 100'720 x, resulting in a pixel size of 1.39 Å on the object scale. To improve the resolution and quality of the 28S subunit cryo-EM map limited by conformational and compositional heterogeneity, the previously selected particle population (roughly 141'700 particle images (14)) was addressed by 3D classification in RELION (44) using limited angular searches ($\sigma_{\text{Angles}} = 4.0^\circ$, angular step size 3.75°) and full-size images (1.39 Å/pixel on the object scale). A mask was applied to remove the density for the large subunit and focus the classification on the small subunit. This led to the identification of a sub-population of roughly 78'800 particle images exhibiting occupancy with tRNAs and density for the region attributed to mS39 (Fig. S1A). These particle images were refined to high resolution in RELION (44) by isolating the 28S subunit by computational masking, thereby focusing the alignment on the 28S subunit. This resulted in a 3.6 Å resolution reconstruction of the 28S subunit according to the Fourier Shell Correlation (FSC) = 0.143 criterion (Fig. S1B) that could be used for manual atomic model building, refinement, and validation.

Notably, by this focused alignment procedure the quality of our 3.6 Å reconstruction of the 28S subunit from 78'800 particle images was markedly improved compared to the density of the 28S subunit portion of the 55S mitoribosome reconstruction from 141'700 particles reported previously (14). Within this initial 55S mitoribosome reconstruction, the 28S subunit part was only resolved to 4.1 Å on average, precluding its interpretation with an atomic model (14). While our improved density map allowed atomic model building for most parts of the 28S subunit, regions of lower local resolution near mS27 and mS39 (Fig. S1C, D) were interpreted only as poly-serine α -helices.

The components built in our 28S subunit structure are provided in Table S3. We were able to locate and build all proteins assigned to the 28S subunit, including mS37 (CHCHD1) and mS38 (AURKAIP1), which have been identified as mitoribosomal proteins only recently (3). Although previous mass-spectrometric identifications and a lower-resolution model of the 28S subunit predicted the presence of three additional

proteins in the 28S subunit (4, 16), we identified two of these as components of the 39S large mitoribosomal subunit (14), and MRPS36 has recently been reassigned as a component of the α -ketoglutarate dehydrogenase complex (45). Our structure shows only modest agreement with a previous lower-resolution model of the 28S subunit (16).

Particle sorting for analysis of the mRNA gate region

The particle subpopulations used for the analysis of structural heterogeneity of the mRNA gate region (Fig. 4C, D) were identified by 3D classification in an approach similar to the one described above, using full-sized particle images and limited angular searches (Fig. S1A). However, in this case, the maximum resolution of the data considered for refinement was strictly limited to 15 Å, effectively focusing the classification on intermediate-resolution features and precluding contributions from high-resolution features to the classification. For comparison of the mRNA gate features, two subpopulations were chosen and refined to higher resolution: The single class without bound tRNAs (14'302 particles, final resolution 6.3 Å), and the class with the most clearly defined A- and P-site tRNAs and a well-ordered mRNA gate (22'364 particle images, final resolution 4.2 Å). For comparison of their features (Fig. 4C, D), the maps were low-pass filtered to the same 6.5 Å resolution.

Calculation of 55S cryo-EM reconstructions

Our previous reconstruction of the 39S mitoribosomal subunit was based on a particle population that could be successfully refined to obtain a structure of the entire 55S mitoribosome at a nominal resolution of 3.6 Å (14), while the 28S subunit in this reconstruction was resolved to only 4.1 Å resolution (14). Re-evaluation of existing 3D classes obtained during data processing for the 39S subunit structure (14) indicated the presence of conformational flexibility of the 28S subunit relative to the 39S subunit in this particle dataset (Fig. S3). Therefore, two particle subpopulations of roughly 60'900 and 30'500 particles were selected and refined independently to yield structures of the 55S mitoribosome at 3.8 Å and 4.2 Å resolution, respectively (Fig. S3A-D). The better resolved cryo-EM map corresponds to a mitoribosome in the canonical state with classical A- and P-site tRNAs and was used for the subsequent refinement of the atomic model of the 55S mitoribosome. In the second cryo-EM map, the 28S assumes a different conformation relative to the 39S subunit, and the density for the P-site tRNA is considerably weaker, indicative of lower occupancy and increased flexibility of this tRNA in this particle population. The density for the P-site finger is also weaker in this reconstruction, likely for the same reasons.

Atomic model building, structure refinement, and validation

The atomic model of the 28S subunit was built using O (46, 47) and Coot (48) and subsequently refined and validated using PHENIX (49) as described (14). In short, after one round of rigid-body refinement using individual proteins, rRNA domains, tRNAs and the mRNA as rigid groups, the manually built model was subjected to 9 cycles of individual coordinate and B factor refinement against the structure factors and phases calculated from the experimental EM map and using the mlhl refinement target function (14). Based on the refinement statistics of individual resolution shells, coordinate refinement was limited to 3.7 Å resolution (Table S2), but the refined model and map

show meaningful correlation beyond this resolution (Fig. S1B). For maintaining good main-chain geometry in areas of lower local resolution, Ramachandran-, secondary structure-, and base pair-restraints were automatically detected by PHENIX and used throughout. For proper coordination of the Zn^{2+} ions in zinc binding proteins and the Mg^{2+} bound to the GDP, custom bond and angle definitions were applied, while two possible disulfide bridges were detected automatically. Magnesium ions coordinated by the rRNA were picked after inspection of the initial $F_{\text{obs}}-F_{\text{calc}}$ difference Fourier map and added to the input model for re-refinement. The final refinement and model statistics are given in Table S2, and the B-factor distribution in the refined molecular model is shown in Fig. S2A, B.

In order to avoid over-refinement, we established the optimal weighting of the model geometry against the experimental data by screening different constant settings of the “crystallographic” refinement target. For this, we used the `fix_wxc` option implemented in PHENIX (50). The program then ignores the automatically determined coordinate refinement weights and simplifies the refinement target function for restrained refinement of individual coordinates to:

$$E_{\text{total}} = \text{fix_wxc} \cdot E_{\text{xray}} + E_{\text{geom}}$$

E_{geom} represents the sum of geometry restrains (including secondary structure and Ramachandran restrains), and E_{xray} is the crystallographic refinement target (here, phased maximum likelihood (mlhl) was used). A value of `fix_wxc` = 1.1 resulted in a quality of model geometry and R-values typical for this resolution range (51) (Table S2). Higher values of `fix_wxc` resulted in lower R-factors but worse model geometry and possible overrefinement, while lower values of `fix_wxc` lead to higher R-factors but overtightened model geometry. For structure validation, the final model was re-refined against the two half-set maps as described above after applying a random coordinate shift of 0.5 Å and resetting the B factors to remove potential model bias (Fig. S2C and also see (14)).

The refinement of the 55S molecular model was based on the fully refined coordinates of the 39S and 28S subunits at higher resolution, which were fitted into the 3.8 Å and 4.2 Å cryo-EM reconstructions of the 55S mitoribosome (Fig. S3) by rigid body refinement using large segments (head and body of the 28S subunit; core area, central protuberance and L7/L12 stalk of the large subunit). At the interface of both subunits, two areas of protein contacts were manually rebuilt in the 3.8 Å map, unassigned α -helices representing the P-site finger were added, the tRNA fragments originating from both subunits were connected and readjusted, and coordinated magnesium ions at the subunit interface were added. The complete model was then fully refined against the 3.8 Å cryo-EM map using PHENIX (Table S2; Fig. S2D-F) in a similar procedure as described above for the 28S subunit, except for the B factor, which was refined in group-wise mode (two groups per residue after resetting it to a start value of 80 Å²) and the geometry weighting term (`fix_wxc` = 1.3). Further, the coordinated magnesium ions at the subunit interface were also included during refinement. Because the mRNA and tRNAs bound in the intersubunit space correspond to a heterogeneous mixture to which no specific sequence can be assigned, these RNA molecules were modeled as poly-pyrimidine, with the exception of the codon-anticodon interaction,

where purine-pyrimidine base pairs were built. Poly-pyrimidine modeling was chosen to preserve the information regarding positioning and orientation of the nucleoside base contained in our cryo-EM maps, which would be lost if only a phosphate backbone trace were deposited.

Mass spectrometry experiments

Chemical crosslinking using *S. scrofa* 55S mitoribosomes and analysis of crosslinked and non-crosslinked *S. scrofa* 55S ribosomes using LC-MS/MS was performed as described (14). The results of the CX-MS experiments are listed in Table S1, and crosslinks mapped to the structure are shown in Fig. S6. The results of the mass-spectrometric identification of 28S subunit protein isoforms in our mitoribosomal sample are provided in Additional Data Table S1 (presented as a dedicated spreadsheet file).

The N-terminus of protein mS38 is embedded in the 12S rRNA in an arrangement that is incompatible with the presence of full-length mS38. However, this assignment is supported by the high quality of the density in this area, where side chains can be clearly recognized. In agreement with the hypothesis that the N-terminus of mS38 is absent, possibly due to post-translational processing, our mass spectrometric analysis detected peptides only for the C-terminal half of the protein (starting at residue K129, see Table S7). An independent study also detected only peptides near the C-terminus and found mS38 to run at lower molecular weight than expected for the full-length protein in SDS-PAGE gels (3).

Nomenclature of intersubunit bridges

The nomenclature for intersubunit bridges is derived mostly from the bacterial 70S crystal structures (17, 52) and the initial mitoribosomal bridge nomenclature introduced in ref. (5). Bacterial intersubunit bridges are subdivided into 8 bridge groups (B1-B8) (17). This group numbering has been adopted here, along with the mitoribosomal-specific bridge group B9 (5).

The subdivision of groups into individual bridge elements denoted by suffix letters (a-f) has been adopted from ref. (5) if possible, and mostly does not correspond to the nomenclature used for bacterial ribosomes, as many bridge elements have been exchanged in mitoribosomes. Additional elements as compared to ref. (5) have been added as required and are denoted with additional suffix letters.

Calculation of buried surface area

Buried surface area of the mS29-28S subunit interaction was calculated using PDBeFold (53).

Creation of figures

Figures depicting molecular structures were created using the UCSF Chimera package from the Computer Graphics Laboratory, University of California, San Francisco (supported by NIH P41 RR-01081) (54) and PyMOL (The PyMOL Molecular Graphics System, Version 1.7 Schrödinger, LLC.). Local resolution plots were generated in ResMap (55).

Supplementary Text

Intersubunit bridges in the 55S mammalian mitoribosome

Mitochondrial-specific ribosomal protein elements are involved in the formation of several intersubunit bridges, including B1, B2, and B9, possibly to compensate for interaction surfaces lost due to rRNA reduction or altered conformation of components of bacterial intersubunit bridges.

The B1 bridge group between the central protuberance (CP) of the 39S subunit and the head domain of the 28S subunit is likely functionally equivalent to the corresponding bacterial bridges, but involves mitochondrial-specific ribosomal proteins mS29, mL46, and mL48 due to the remodeling of both the 39S CP and the 28S subunit head (Fig. S4G, H). mS29 as well as h42 of the 12S rRNA of the 28S head form the B1b-B1d contacts to proteins mL46 and mL48 of the 39S subunit CP (Fig. S4G). These interactions replace the contacts of the 50S proteins bL31 and uL5 to the 30S protein uS13 in bacterial ribosomes, the latter two of which are absent in the mammalian mitoribosome (Fig. S4G, H). The density in this region could not be fully interpreted due to low local resolution. Therefore, less well ordered parts of additional proteins, including bL31m and mL40, may also be involved in intersubunit interactions near the position of bacterial B1a, where the cryo-EM density for an α -helix is present, which however could not be unambiguously connected to one of the large subunit proteins in this region.

Other bridge groups that have been strongly remodeled due to loss of mitoribosomal rRNA components are B4 (loss of 16S H34), B6 (loss of 16S H62), and B8 (loss of 12S h14). Remaining 12S rRNA near bridges B6 and B8 may form loose interactions with 39S subunit proteins in the structure of the 55S mitoribosome when the 28S subunit body is tilted towards the 39S subunit. Indeed, the absence of full bacterial-like B6 and B8 contacts may be the reason why we observe 28S subunit tilting, as the presence of these bridges would stabilize the interface between the two subunits and may sterically exclude 28S subunit tilt towards the 39S subunit. B7a is probably also weakened due to truncation of 16S H68, however unassigned density features in this region indicate the presence of an intersubunit contact possibly involving the remaining rRNA.

The pivot point of intersubunit rotation in the bacterial ribosome is located near bridge group B3 (56). In the immediate vicinity of B3, the mitoribosomal-specific protein mS38 is partially embedded in a cavity of the 12S rRNA (Fig. 1C; Fig. S4I), similarly to the eukaryotic-specific cytosolic protein eL41 (57). mS38 is involved in formation of bridges B2c, B2d, and B2f near the center of the subunit interface. The position of mS38 in the 39S subunit partially overlaps with the position of the bacterial 23S rRNA helix H62 in the 70S ribosome, and its interactions with the large subunit might partially compensate for the loss of the H62-h44 interaction (parts of B5 and B6 (17)) in the mammalian mitoribosome (Fig. S4J).

B9 is a mitoribosomal-specific bridge at the foot of the 28S subunit, where an extended tail of bL19m reaches across the solvent space between the two subunits and contacts mS27 (Fig. S4K) in a fashion reminiscent of the interaction of the 60S subunit protein eL24 with the eukaryotic cytosolic 40S ribosomal subunit (57).

Comparison of the mitoribosomal tRNA binding sites to bacterial ribosomes

As detailed in the main text, a number of ribosomal elements involved in interactions with the A- and P-site tRNAs have been lost in mammalian mitoribosomes

and are partially compensated for by the P-site finger. The main differences between the bacterial and mitoribosomal A- and P-site tRNA binding sites are briefly discussed below.

In bacterial ribosomes, the small subunit protein uS13 binds to the A- and P-site tRNA anticodon stem loops (ASLs) (*18*). In the mitoribosomal 28S subunit, this protein has been lost (Fig. 2C; Fig. S4G, H), and the binding of these tRNAs is mediated mostly by the remaining conserved interactions with the 12S rRNA and the C-terminus of uS9m (Fig. 2C, D).

On the 39S subunit, the interactions with the tRNA elbow regions have been weakened by the loss of the A-site finger (H38) and bL25 in the A-site, and by the absence of uL5 in the P-site (*14, 15*). While the P-site finger (Fig. 2A, B, D) probably compensates for a part of these missing interactions (see main text), the P-site tRNA elbow appears to be relatively flexible and correspondingly shows weaker density in our cryo-EM maps. This indicates that the P-site finger, being a relatively flexible structure itself, may not provide the same level of conformational stabilization as direct interactions with rigid large ribosomal subunit components. The A-site tRNA elbow appears to be better ordered in our cryo-EM maps, probably due to its interactions with uL16m (Fig. 2B, D, E).

The interactions critical for tRNA selection and peptide bond formation, which involve mostly rRNA near the decoding site and the active center of the ribosome, are highly conserved in the 55S mitoribosome (Fig. 4 and (*14*)).

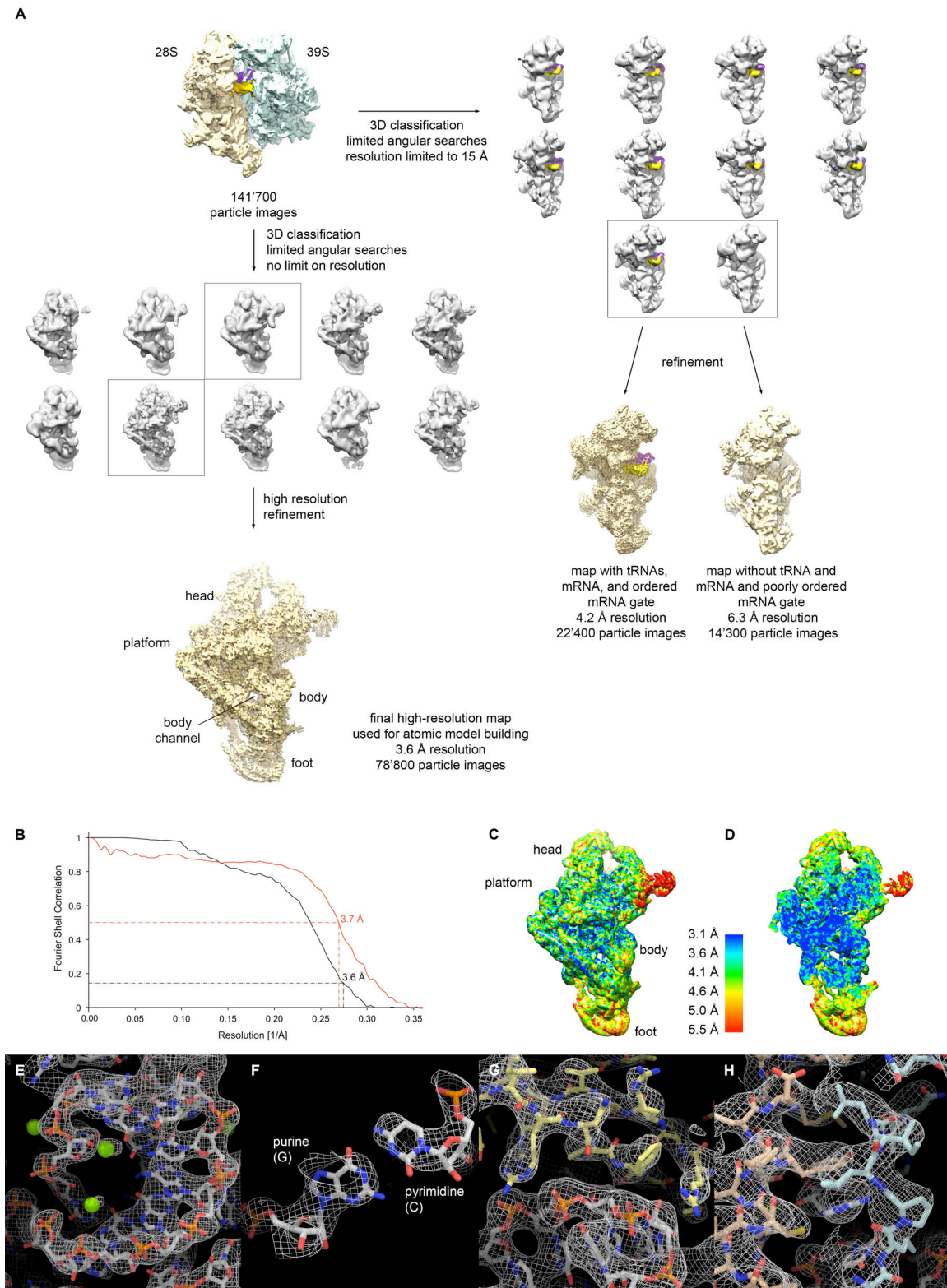


Fig. S1.

Computational sorting of the 55S mitoribosome dataset for 28S subunit structure determination and cryo-EM map of the 28S subunit. (A) A pre-sorted 55S

mitoribosome dataset (14) was subjected to further 3D classification to reduce heterogeneity of the 28S subunit data, which had previously compromised the quality of the 28S subunit density in a map of the 55S mitoribosome (14). Classification using limited angular searches but no restrictions on resolution (left) was used to sort the data prior to high-resolution refinement. Classes that showed weak density for tRNAs or for the region attributed to mS39 at the head were discarded. 2 classes (indicated by boxes; roughly 78'800 particles) out of a total of 10 classes (roughly 141'700 particles) were selected for high-resolution refinement, resulting in a 3.6 Å map of the 28S subunit. The remaining 8 classes showed weak or fragmented density for peripheral regions of the 28S subunit. Classification using limited angular searches and a resolution cut-off of 15 Å (right) was used to classify for differences in intermediate-resolution features and allowed the analysis of the structural heterogeneity of the mRNA gate (Fig. 4C, D). **(B)** Black: Fourier Shell Correlation (FSC) curve ("gold standard" (58)) of the 28S subunit cryo-EM map with an estimated resolution of 3.6 Å according to the FSC = 0.143 criterion (59). Red: FSC curve computed from the final cryo-EM map and the refined coordinates. The FSC = 0.5 criterion has to be used in this case (59). **(C, D)** Local resolution plots of the 28S subunit map. While the core region is likely resolved beyond the nominal resolution of the map, some peripheral regions are less well ordered and exhibit lower local resolution. **(E-H)** Close-up views of the cryo-EM density shown with the underlying refined atomic model. **(E)** rRNA helix with bound magnesium ions. **(F)** G-C base pair. Purines can be clearly distinguished from pyrimidines. **(G)** Stretch of ribosomal protein (light yellow) interacting with the phosphodiester backbone of the 12S rRNA (light grey). **(H)** Protein α -helix (light brown) interacting with a second protein strand (light blue) and forming a stacking interaction with the 12S rRNA (light grey).

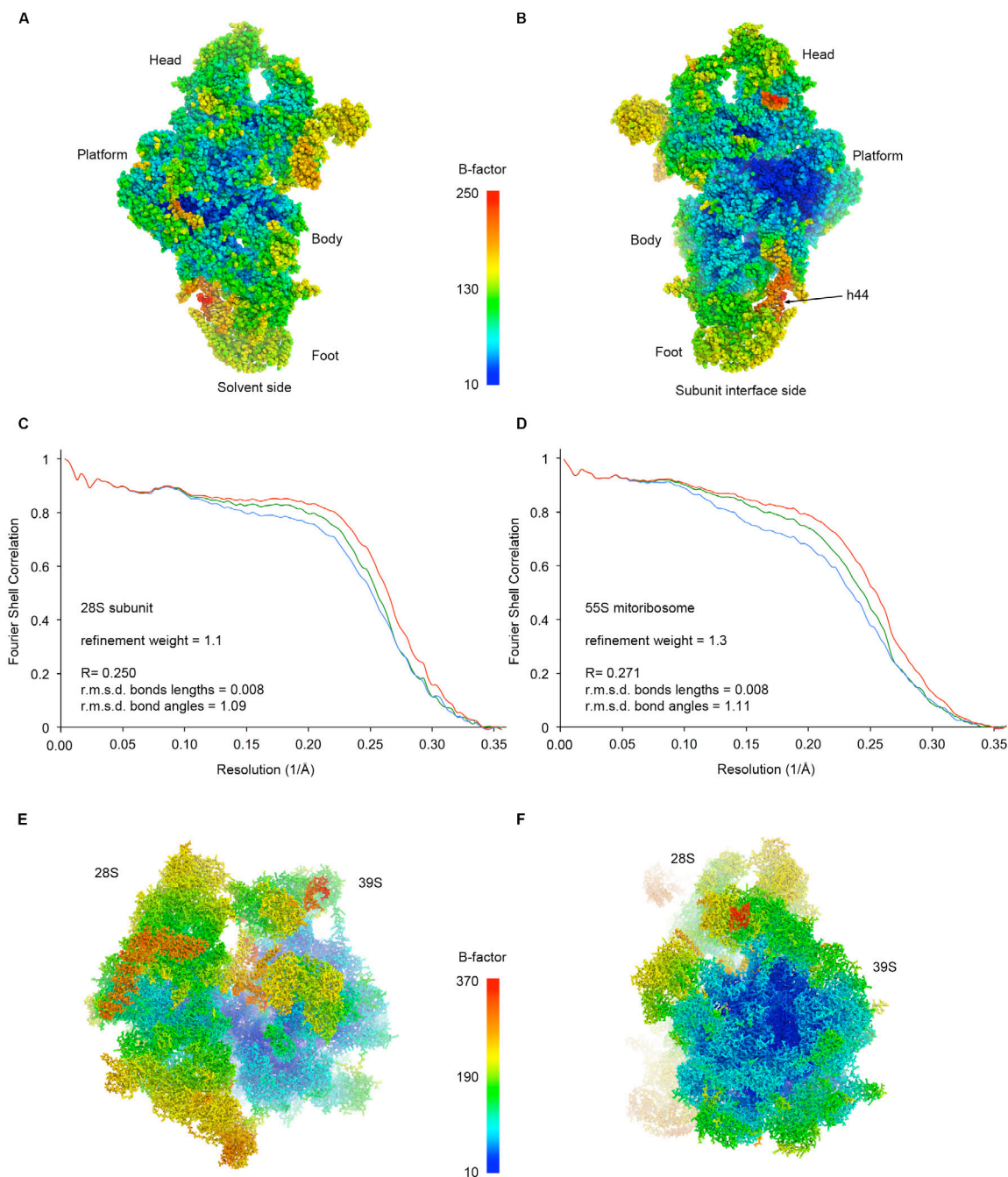


Fig. S2

Coordinate refinement of the 28S subunit and 55S mitoribosome atomic models. (A, B) The 28S subunit structure colored according to B factors obtained during coordinate refinement. The distribution of B factors indicates that the rRNA core is very well ordered, while some peripheral regions, in particular the distal end of h44, exhibit greater mobility and correspondingly higher B factors. (C) Refinement weight parameter validation for the 28S subunit refinement. For validation purposes, the atomic coordinates were randomly displaced by 0.5 Å and then re-refined into the cryo-EM map obtained

from one half of the data. Model versus map FSC curves are shown (red: FSC model versus map calculated from all particle images; green: FSC model versus map calculated from data half-set 1 (used for refinement); blue: FSC model versus map calculated from data half-set 2 (not used for refinement). A large gap between the green and blue curves would be indicative of over-refinement (for details see Methods). **(D)** As in **(C)** but for the 55S mitoribosome atomic coordinate refinement. **(E, F)** B factor distribution in the 55S mitoribosome structure (**E**, side view; **F**, 39S subunit solvent side view). The 39S subunit exhibits lower B factors in general compared to the 28S subunit, and the tRNAs in the intersubunit space exhibit relatively higher B factors.

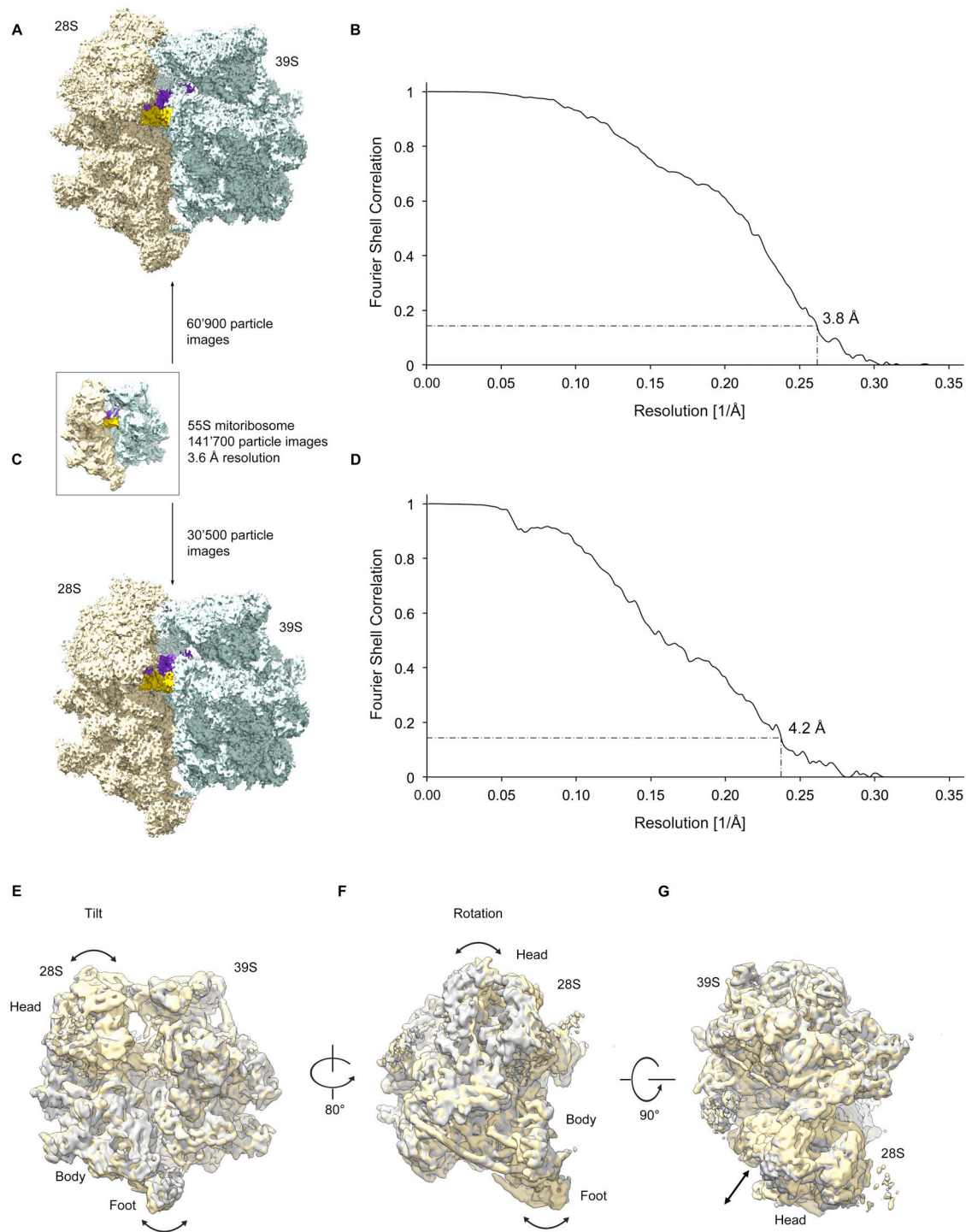


Fig. S3

Cryo-EM reconstruction of the 55S mitoribosome. (A, B) Overall structure of the 55S mitoribosome in the canonical state with classical A- and P-site tRNAs at 3.8 \AA resolution (FSC = 0.143 criterion (59), “gold standard” (58)) calculated from approx. 60'900 particle images. The inset represents the previous 3.6 \AA map computed from the full 141'700-particle dataset (14). (C, D) Overall structure of the 55S mitoribosome in a

conformation similar to the canonical state, but with an additional tilt of the 28S subunit, at 4.2 Å resolution (FSC = 0.143 criterion, “gold standard”) calculated from approx. 30’500 particle images. **(E-G)** Comparison of the two mitoribosomal substates exhibiting different subunit tilt, shown in side view (**E**), 28S subunit view (**F**), and top view (**G**). Conformational differences between the two 28S subunit conformations are indicated with bold arrows (superposition of the 55S mitoribosome reconstructions based on the 39S subunit). The intersubunit movement observed can not be fully explained by the classical intersubunit rotation (56, 60, 61), but additionally involves a rotation around an axis that traverses the 28S subunit approximately along the mRNA channel, resulting in tilting of the 28S subunit. This 28S subunit tilting causes changes in the distance between the 28S subunit body and the 39S subunit foot, as well as between the 28S subunit head and the 39S subunit CP (also see Fig. S5). 28S subunit tilting also changes the distance between the elongation factor binding site on the 28S subunit and the Sarcin-Ricin Loop on the 39S subunit, which has been observed previously in mammalian cytosolic ribosomes performing a rolling movement (62). However, the axis of rotation appears to be different between subunit rolling in cytosolic ribosomes and subunit tilting in mitoribosomes.

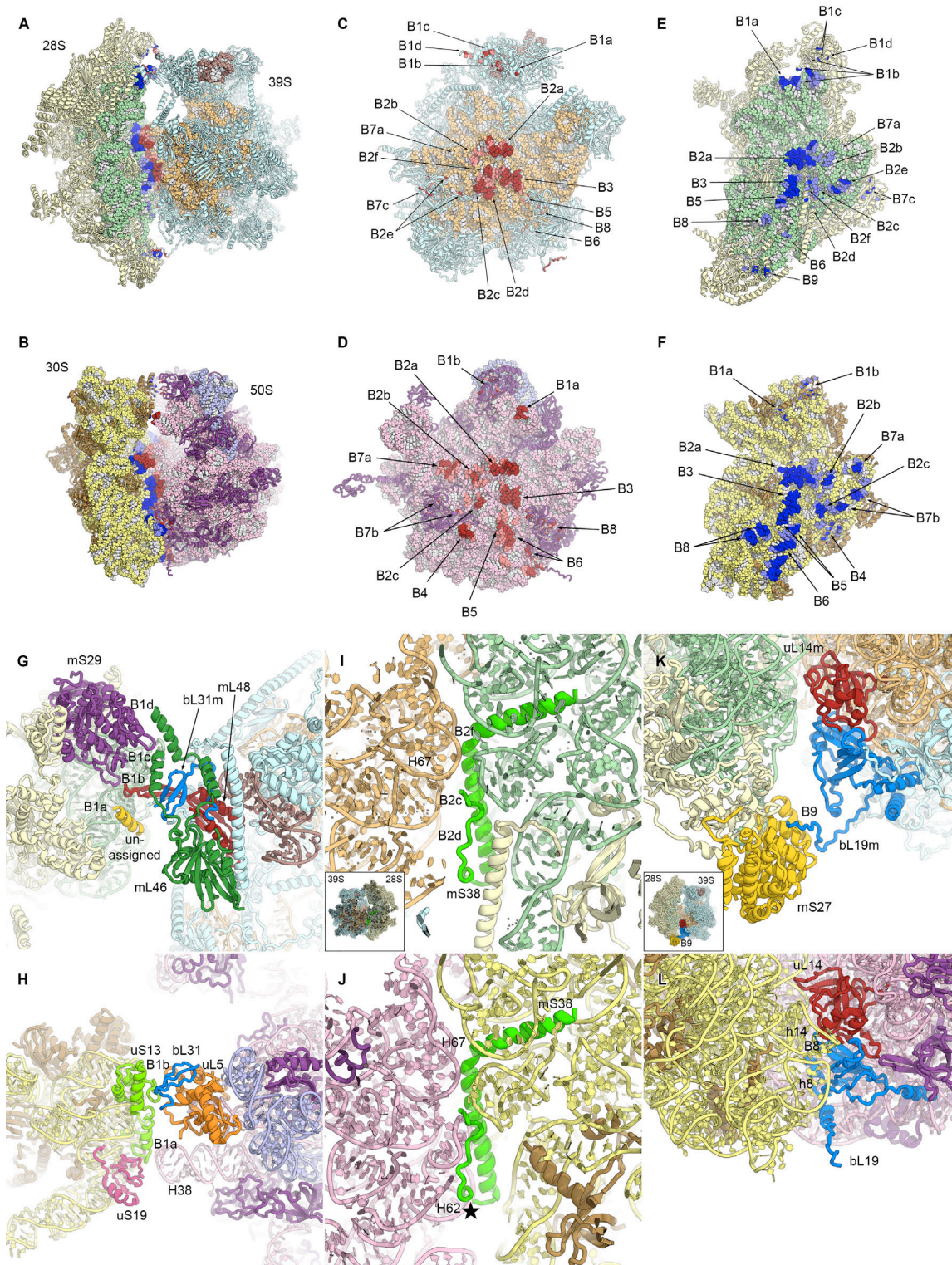


Fig. S4.

Intersubunit bridges in the 55S mitoribosome and comparison to the bacterial ribosome. (A-F) Comparison of mitoribosomal intersubunit bridges (A, C, E) and bacterial intersubunit bridges (17, 18) (B, D, F). Intersubunit bridges (distance $< 4 \text{ \AA}$) are

colored red (large subunit) and blue (small subunit), elements in close proximity ($< 6 \text{ \AA}$) in light red (large subunits) and light blue (small subunits). Color code: 39S subunit proteins cyan, mitochondrial 16S rRNA light orange, 28S subunit proteins pale yellow, 12S rRNA light green, 50S subunit proteins purple, 23S rRNA pink, 30S subunit proteins brown, bacterial 16S rRNA yellow. **(G-L)** Detailed comparison of intersubunit contacts in the 55S mitoribosome at the top (**G, I, K**) and bacterial ribosomes at the bottom (**H, J, L**). Colors as in **(A-F)**. **(G)** Contacts at the mitoribosomal CP (mL46 green, mL48 dark red, mS29 purple, bL31m blue). Bridges of the B1 group are located in similar regions of the structure as in bacterial ribosomes (**H**), however, their molecular components have mostly been exchanged due to loss of uS13 (bright green) and shortening of H38 in the mitoribosome. **(I)** View of mS38 (bright green) bound in a pocket of the 12S rRNA and forming contacts B2c, B2d, and B2f with the 16S rRNA. **(J)** In the bacterial ribosome, the position of mitoribosomal mS38 (superposed from 28S subunit coordinates, bright green) overlaps with the 23S rRNA H62 region (star). **(K, L)** Interactions in the 28S lower body region (mS27 in gold, uL14m in red, bL19m in blue). Bridge B8 formed by bacterial h14 (**L**) is strongly reduced in the mitoribosomal 12S rRNA (**K**), but might be partially compensated by the mitochondrial-specific bridge B9 (**K**), which is formed by an extension of bL19m and mS28.

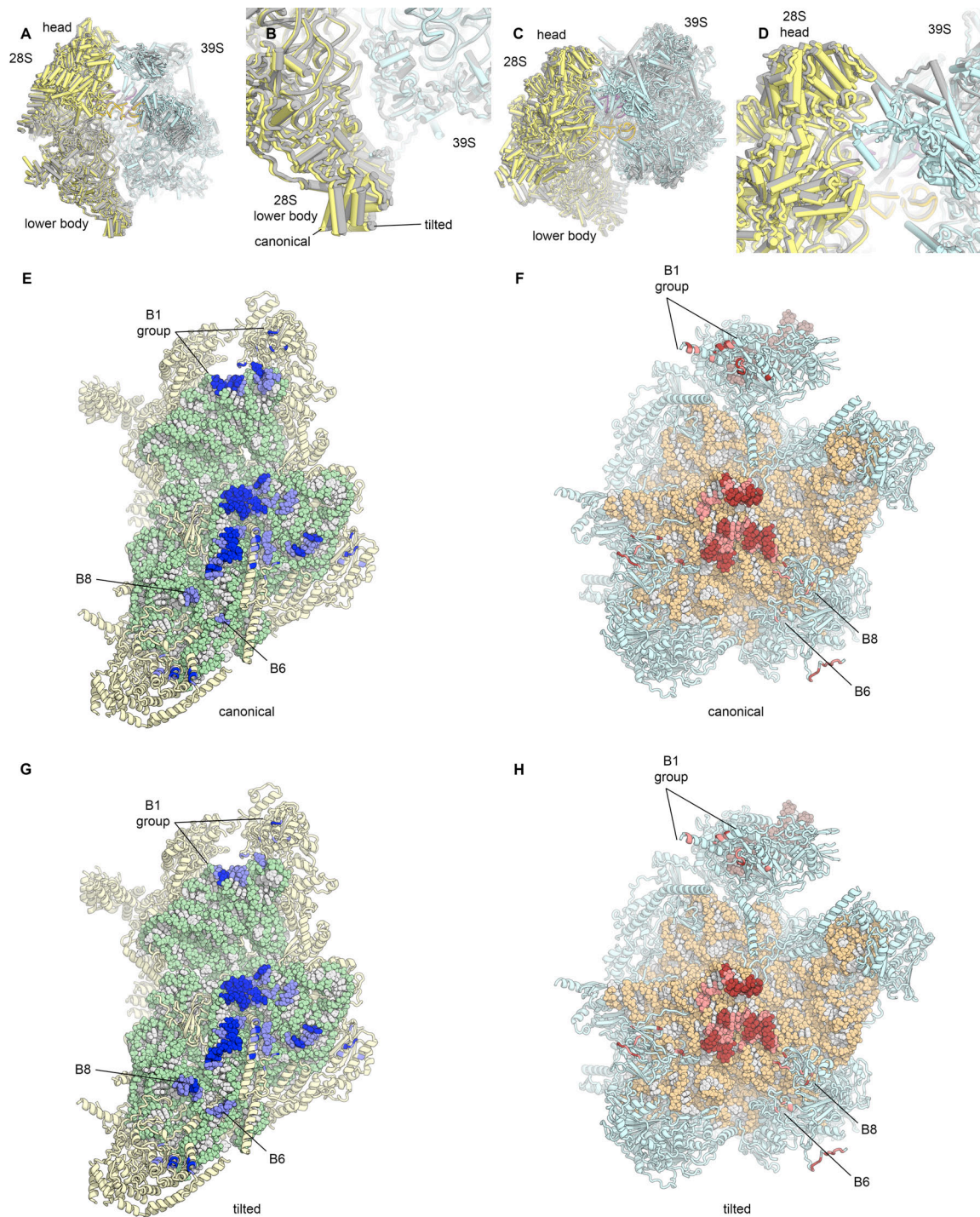


Fig. S5

Comparison of intersubunit contacts in the 55S mitoribosome in the canonical state and the tilted conformation. (A) Side view of the 55S mitoribosome (canonical conformation colored: 39S cyan, 28S yellow, A-site tRNA gold, P-site tRNA purple; tilted conformation grey). **(B)** View of the lower body region of the 28S subunit. Tilting moves the lower body of the 28S subunit towards the 39S subunit. **(C, D)** The head of the

28S subunit moves away from the CP in the tilted conformation. **(E, F)** Intersubunit bridges of the 55S mitoribosome in the canonical state (for details see Fig. S4). **(G, H)** Intersubunit bridges in the tilted conformation. Some interactions of the B1 bridge group at the 28S subunit head are loosened, while bridges B6 and B8 of the 28S subunit body gain some contact area. Subunit tilting is likely enabled by the reduction of several bridge groups in the 28S subunit lower body, including B5, B6, and B8, which, when present, may prevent such movements from occurring.

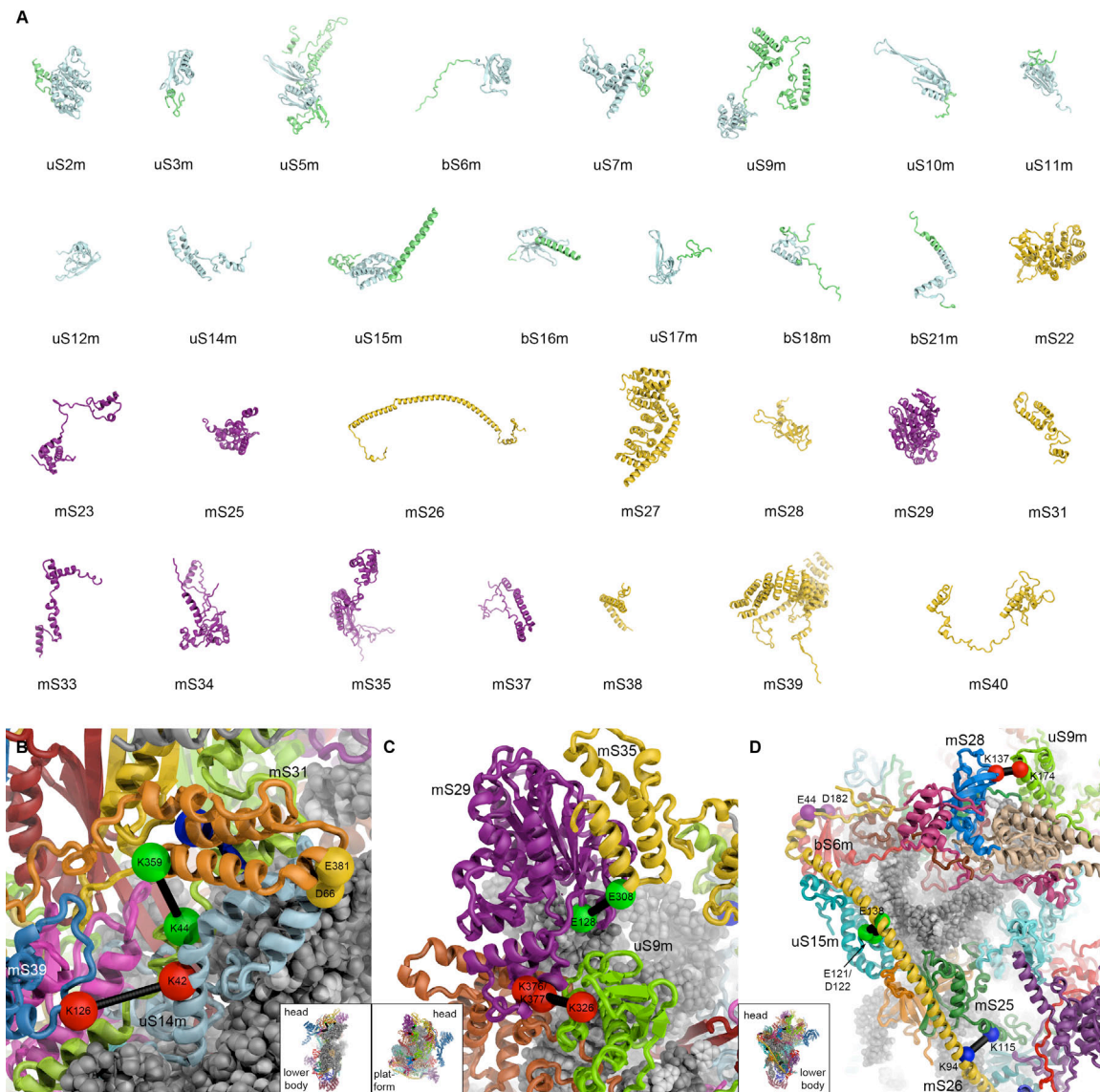


Fig. S6

Proteins of the 28S subunit. (A) Overview of the structure of all 28S subunit proteins colored according to conservation (cyan: conserved bacterial ribosomal proteins, with their mitochondrial-specific extensions in green; purple: mitochondrial-specific ribosomal proteins, yellow: mitochondrial specific ribosomal proteins not present in fungal mitoribosomes). (B-D) CX-MS crosslinks used to identify mitochondrial-specific ribosomal proteins or confirm their locations (C_{α} of crosslinked residues shown as spheres). See also Table S1.

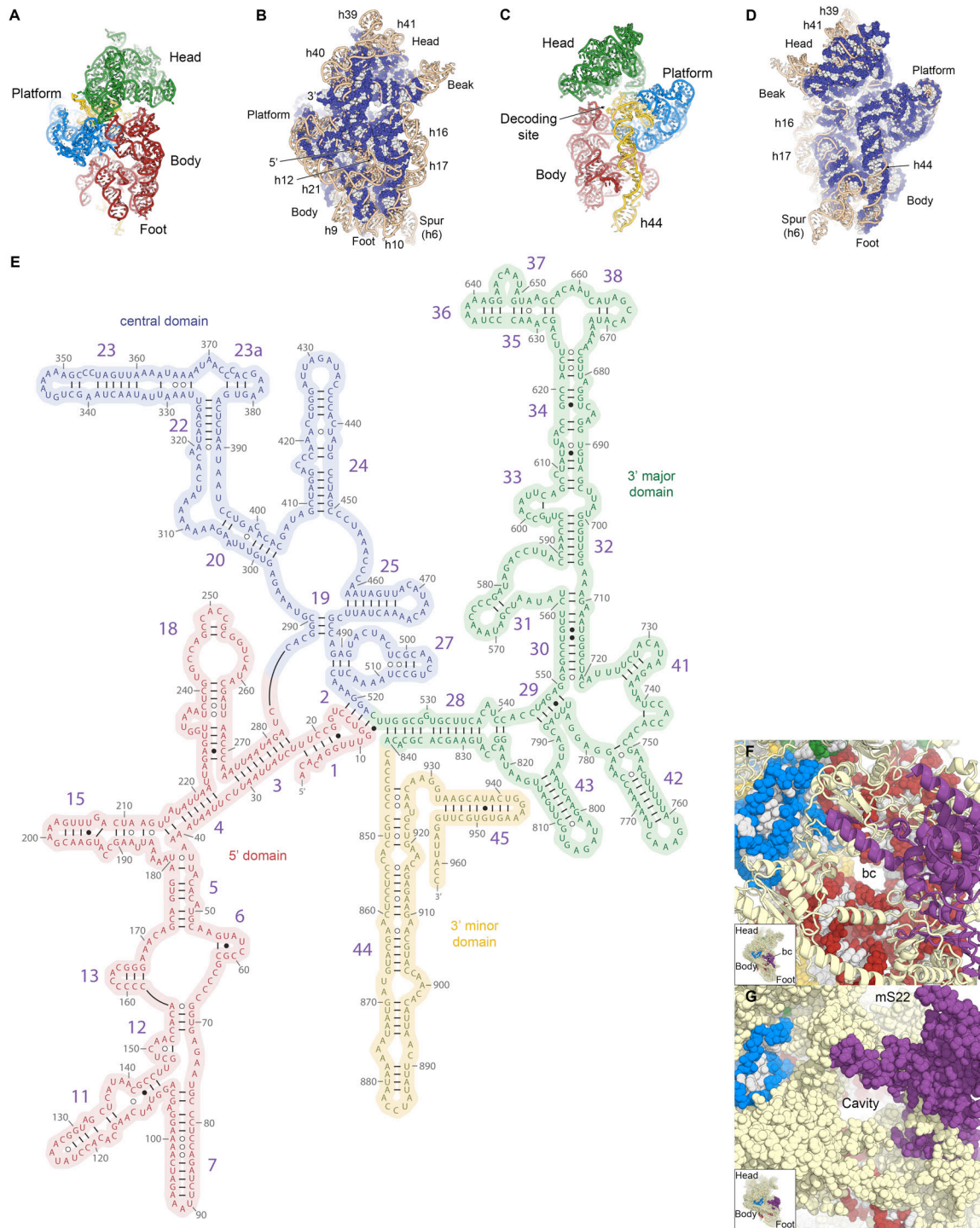


Fig. S7.

Structure of the 12S rRNA. (A-D) Views of the 12S rRNA (A, C: 5' domain in red, central domain in blue, 3' major domain in green, 3' minor domain in yellow; B, D: shown as spheres, backbone dark blue, bases white) from the solvent side (A, B) and the subunit interface side (C, D). The structure of the bacterial 16S rRNA (18) is shown as overlay in light brown for comparison in (B) and (D). Landmarks of the 28S subunit and

the 12S and 16S rRNAs as well as the major rRNA helices missing in the 12S rRNA are labeled. (E) Secondary structure diagram of the 12S rRNA. The major secondary structure domains of the 12S rRNA are labeled and delineated in color. Depiction based on the secondary structure diagram of the bacterial 23S rRNA (17) (template obtained from the Noller lab web page http://rna.ucsc.edu/rnacenter/noller_lab.html). (F) Due to the loss of bacterial h12, a channel through the 28S subunit has appeared (rRNA as in A, ribosomal proteins in yellow, mS22 in purple). (G) On the solvent side of the subunit, this channel widens into a cavity located below mS22 (purple).

donates the fourth zinc binding cysteine. This suggests that these interactions are important to structurally stabilize the rapidly evolving mitoribosomal proteins and their quaternary interactions. **(G)** Sequence alignment of bS18 homologs in *E. coli*, *T. thermophilus*, and *S. scrofa* mitochondria. The position of cysteines involved in Zn^{2+} -binding in all porcine bS18 homologs is indicated with stars. An arrow denotes the position of the fourth Zn^{2+} -binding cysteine in mS40.

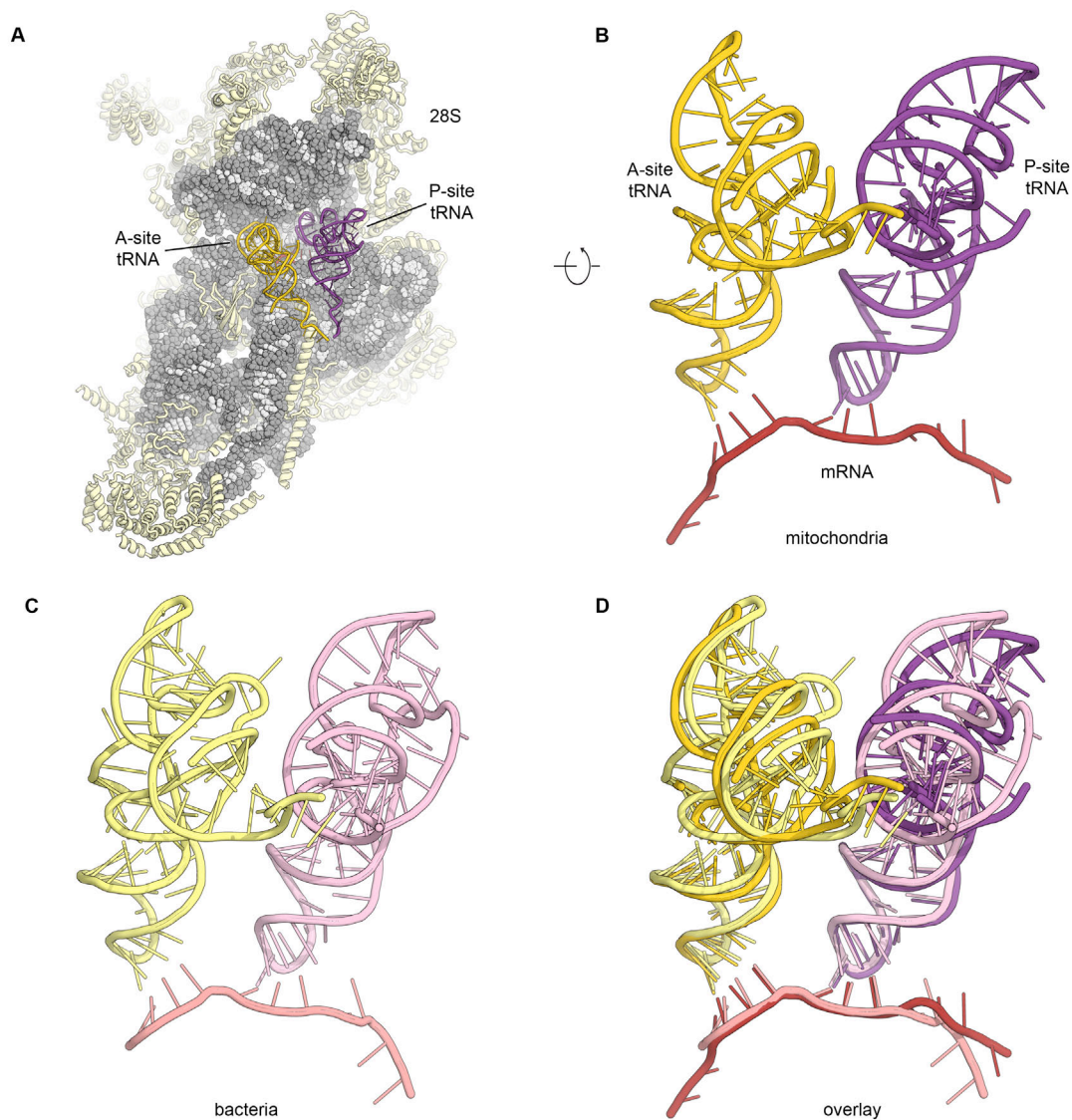


Fig. S9

Comparison of the mRNA path and mRNA-tRNA interactions in the 28S subunit.

(A) Overview of the 28S subunit with bound mRNA and tRNAs. (B) Depiction of mRNA and tRNA in the mammalian 55S mitoribosome. The view is tilted upwards to reveal the mRNA. (C) As in B, but for the bacterial ribosome (PDB ID 2WDK) (18). (D) Overlay of B and C. The conformation of the mRNA and its interactions with the tRNAs are highly conserved between the bacterial ribosome and the mammalian mitoribosome.

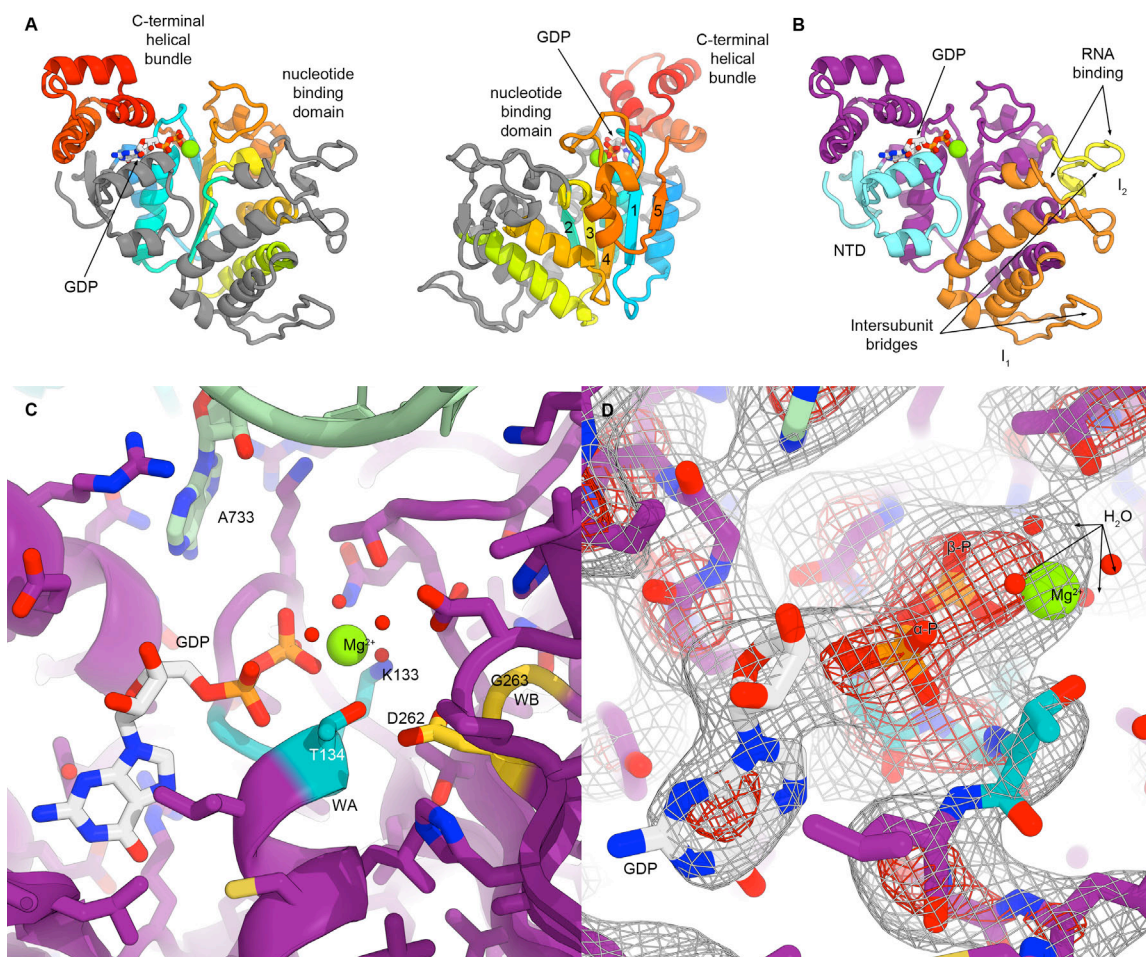


Fig. S10

The overall fold and the guanine-nucleotide binding pocket of mS29. (A) Two views of the topology of mS29 with the conserved AAA+ ATPase-like core colored using a gradient from blue (N terminus) to red (C terminus) and β -sheets numbered according to their appearance in the protein sequence (GDP molecule in white). (B) The N-terminal domain (NTD) and two insertions (I_1 , I_2) of mS29 (purple) are colored in cyan (NTD), orange (I_1), and yellow (I_2). The NTD is involved in shielding of the nucleotide binding pocket, while the extensions participate in RNA binding and intersubunit bridge formation. (C) The nucleotide binding pocket of mS29. The conserved Walker A-motif is shown in dark cyan, key residues are indicated. The Walker B-motif, lacking the second acidic residue in position 263 (replaced by glycine) is shown in yellow. 12S rRNA (green) nucleotide A733 inserts into the mS29 fold near the nucleotide binding pocket. (D) Density in the mS29 nucleotide binding pocket indicates the presence of a GDP molecule.

Table S1.

CX-MS crosslinks used for confirmation of protein localizations. Peptides: crosslinked peptides including location of the crosslinked residues in the peptides; Protein/residue: protein name and residue number of crosslinked amino acids; M_r : theoretical molecular mass of the crosslink product; m/z : experimentally determined mass-to-charge ratio; Id score: identification score calculated by xQuest; DSS: disuccinimidyl suberate; PDH: pimelic acid dihydrazide.

Peptides	Protein/ residue	Protein/ residue	M_r (Da)	m/z	Id score
DSS					
LGKHDMTCAVSGGGR-	uS9m	mS29	2801.43	701.365	33.29
KELLFLSNR-a3-b1	K326	K377			
TDTEATETKAS-YKAALK-a9-b2	bS16m	mS25	1982.998	662.007	29.9
	K133	K164			
FIINSYPKYFQK-	mS39	uS14m	2959.439	987.488	29.52
KMAYEYADER-a8-b1	K126	K42			
ILGKNEETLEKEEQEK-	mS25	mS26	3207.589	802.905	28.07
KAQEDAAEHR-a11-b1	K115	K94			
LLDVEKHHNQLR-YQKGTR-a6-b3	uS9m	mS28	2390.278	598.577	25.83
	K174	K137			
AHTEEGKKELLFLSNR-	mS29	uS9m	3553.776	711.763	24.85
LGKHDMTCAVSGGGR-a8-b3	K377	K326			
HFMEVLTCGLSKNPYLSVK-	mS31	mS33	3717.988	930.505	24.84
VVKLFSEQPLAK-a12-b3	K352	K35			
AFDLFNPNFKSTCQR-	mS23	mS28	3503.692	876.931	24.73
GSPKNVESFASMLR-a10-b4	K93	K76			
LFSEQPLAKR-NPYLSVKQK-a9-b7	mS33	mS31	2401.334	601.341	24.38
	K44	K359			
RPEVDGEKYQK-AKDLLAEK-a8-b2	mS28	uS9m	2372.251	594.071	24.19
	K134	K182			
LGKHDMTCAVSGGGR-	uS9m	mS29	2581.233	646.316	23.93
AHTEEGKK-a3-b7	K326	K376			
EGLVVRPQQKGS-	mS26	uS11m	2651.368	663.85	23.38
LDIEDKEEAR-a10-b6	K203	K51			
PDH					
NEGDNENTLSQYK-YVLYGEK-a6-b6	mS35	mS29	2533.203	845.409	32.35
	E308	E128			
VLENPEDTSSLEAR-QAEEAVLQAR-a7-b4	uS15m	mS26	2824.425	707.114	31.13
	D122	E138			
VLENPEDTSSLEAR-QAEEAVLQAR-a6-b4	uS15m	mS26	2824.429	707.115	30.09
	E121	E138			
DLQEVADEEIASLPR-ESGIQLN-a1-b1	uS14m	mS31	2595.319	866.114	26.35
	D66	E381			
VEEALDSPK-NLENLGER-a6-b7	mS26	bS6m	2082.063	695.029	25.72
	D182	E44			

Table S2.

Refinement table for the coordinate refinements of the 28S subunit and the 55S mitoribosome molecular structures.

Data collection, model refinement, and model validation	28S subunit	55S mitoribosome
Data collection		
Particles	78'783	60'872
Pixel size (Å)	1.39	1.39
Defocus range (µm)	0.8-3.4	0.8-3.4
Voltage (kV)	300	300
Electron dose (e ⁻ /Å ²)	20	20
Reciprocal space data		
Spacegroup	P1	P1
<i>a</i> , <i>b</i> , <i>c</i> (Å)	300.24, 300.24, 300.24	355.84, 355.84, 355.84
α , β , γ (°)	90, 90, 90	90, 90, 90
Refinement		
Resolution range (Å)	39.8-3.7	39.8-3.8
Applied geometry weight (wxc)	1.1	1.3
No. reflections	1'117'561	1'716'710
R-factor	0.250	0.271
No. residues		
Protein	5524	13874
RNA	1101	2676
Ligands (Mg ²⁺ /coordinated H ₂ O/ Zn ²⁺ /GDP)	144/118/3/1	351/340/6/1
B-factors overall	74.8	116.8
Protein	82.1	130.5
RNA	61.7	90.8
Ligands (Mg ²⁺ /coordinated H ₂ O/ Zn ²⁺ /GDP)	40.3	57.4
R.m.s. deviations		
Bond lengths (Å)	0.008	0.008
Bond angles (°)	1.09	1.11
Validation		
Protein		
Molprobit clashscore	12.6	15.3
Ramachandran plot		
Favored (%)	96.3	95.8
Allowed (%)	3.6	4.1
Outliers (%)	0.1	0.1
RNA		
Correct sugar puckers (%)	99.1	98.7
Backbone conformation outliers (%)	0	0

Table S3.

Summary of components in the 28S subunit model. These components were used for the molecular structures of both the 28S subunit and the 55S mitoribosome. Nomenclature according to (64).

Protein/RNA	Old name *	Chain ID	Full size [†] (residues)	Modeled residues	Sequence accession code	Structural homologs	Comments
uS2m	MRPS2	B	289	55-274	AK233229.1	uS2	
uS24m/uS3m	MRPS24	C	167	36-167	XP_003134910.1	uS3	
uS5m	MRPS5	E	430	88-106, 122-430	XP_003124867.3	uS5	
bS6m	MRPS6	F	124	2-124	EW168165.2	bS6	Zn ²⁺ binding motif with bS18m
uS7m	MRPS7	G	242	35-242	XP_003131254.1	uS7	
uS9m	MRPS9	I	397	70-177, 195-397	NP_001231482.1	uS9	residues 251-266 built as UNK [‡]
uS10m	MRPS10	J	201	61-189	AK233895.1	uS10	
uS11m	MRPS11	K	196	61-196	NP_001231457.1	uS11	
uS12m	MRPS12	L	139	31-139	AK394439.1	uS12	
uS14m	MRPS14	N	128	28-128	FD598185.1	uS14	
uS15m	MRPS15	O	239	65-239	AK343256.1	uS15	
bS16m	MRPS16	P	135	10-126	XP_003133122.1	bS16	Zn ²⁺ binding motif with mS25
uS17m	MRPS17	Q	130	2-110	XP_003354569.1	uS17	
bS18m	MRPS18C	R	143	47-143 + Zn 500	HX217955.1	bS18	Zn ²⁺ binding motif with bS6m
bS21m	MRPS21	U	87	2-87	XP_003355248.1	bS21	
mS22	MRPS22	a	359	65-356	AK348087.1		residues 309-356 built as UNK [‡]
mS23	MRPS23	b	190	2-136	XP_005669015.1		
mS25	MRPS25	c	173	2-170 + Zn 500	AK346624.1		Zn ²⁺ binding motif with bS16m
mS26	MRPS26	d	205	27-203	XP_001924843.2		
mS27	MRPS27	e	415	336 UNK residues	XP_003134081.1	PPR fold	PPR fold built as UNK [‡]
mS28	MRPS28	f	188	78-176	DN116920.1	OB-fold	
mS29	MRPS29	g	397	52-397 + GDP 500 + Mg ²⁺ 501 + (H ₂ O) 502-505	XP_003361167.1	AAA+ ATPase-like fold	residues 52-69 built as UNK [‡]
mS31	MRPS31	h	387	285-387	XP_001926138.2		
mS33	MRPS33	i	106	4-102	XP_003360155.1		
mS34	MRPS34	j	218	2-214	NP_001231761.1	SH3-like core fold	residues 152-158 built as UNK [‡]
mS35	MRPS35	k	325	51-325	NP_001231856.1	peptidyl-tRNA hydrolase fold	
mS37	MRPS37 (CHCHD1)	m	118	2-117	NP_001177084.1		
mS38	MRPS38/ (AURKAIP1)	n	199	128-199	AK231191.1		N-terminal sequence missing

Table S3 (continued).

Protein/RNA	Old name [*]	Chain ID	Full size [†] (residues)	Modeled residues	Sequence accession code	Structural homologs	Comments
mS39	MRPS39	o	692	55-143 + 387 UNK residues	XP_005662461.1	PPR fold	PPR fold built as UNK [‡]
mS40	MRPS18B	p	258	51-238 + Zn 500	NP_001116612.1	bS18	Zn ²⁺ binding
		s, z		16 + 17 residues			Unassigned helices/folds; built as UNK [‡]
bL19m	MRPL19	T		54-67			terminus of 39S LSU MRPL19 as UNK [‡] ; replaced by chain T in the 55S structure
12S rRNA		A	962	3-962	AP003428.1		
mRNA		X	Mixture of all mt mRNA species	12-24			Modeled based on the structure of the bacterial 70S-mRNA-tRNA complex (18) and deposited as poly-pyrimidine
A-site tRNA		Y	Mixture of all mt-tRNA species	1-15, 21-45, 48-71 ^{&}			Modeled based on the structure of the bacterial 70S-mRNA-tRNA complex (18) and deposited as poly-pyrimidine
P-site tRNA		V	Mixture of all mt-tRNA species	1-15, 21-45, 48-71 ^{&}			Modeled based on the structure of the bacterial 70S-mRNA-tRNA complex (18) and deposited as poly-pyrimidine

^{*} Nomenclature according to the ribosomal protein gene database (65).

[†] Full-length protein sequences including putative mitochondrial targeting peptides.

[‡] Unassigned residues were modeled as poly-serine and deposited as UNK.

[§] Fold predicted by the Phyre2 protein fold recognition server (66).

^{||} PDBeFold search results (67).

[&] In the 55S mitoribosome model, tRNAs include the 3'-terminus (nt. 71-76)

Table S4.

Summary of components in the 39S subunit model. Components used for the molecular model of the 39S subunit in the context of the 55S mitoribosome.

Protein/ RNA	Old name*	Chain ID	Full size [†] (residues)	Modeled residues	Sequence accession code	Structural homologs	Comments
uL1m	MRPL1	-	329	-	AK349766.1	uL1	not visible
uL2m	MRPL2	D	306	61-300	NP_001171996.1	uL2	
uL3m	MRPL3	E	348	42-348	AY609899.1	uL3	
uL4m	MRPL4	F	294	45-294	XP_003123269.2	uL4	
bL9m	MRPL9	I	268	53-150	XP_003355223.1	bL9	
uL10m	MRPL10	J	262	29-196	XP_003131579.1	uL10	Zn ²⁺ binding together with mL66
uL11m	MRPL11	K	192	17-158	XP_003122536.1	uL11	
bL7m/ bL12m	MRPL12	-	198	-	AK234571.1	bL7/ bL12	not visible
uL13m	MRPL13	N	178	2-178	NP_001230344.1	uL13	
uL14m	MRPL14	O	145	31-145	XP_001929596.1	uL14	
uL15m	MRPL15	P	296	9-296	NP_001230457.1	uL15	
uL16m	MRPL16	Q	251	31-251	NP_001231896.1	uL16	
bL17m	MRPL17	R	169	9-161	NP_001231309.1	bL17	
uL18m	MRPL18	S	180	38-180	XP_001928391.1	uL18	
bL19m	MRPL19	T	292	54-292	XP_003354803.1	bL19	residues 54-68 built as UNK [‡]
bL20m	MRPL20	U	149	10-149	XP_003127555.3	bL20	
bL21m	MRPL21	V	209	55-209	AY610123.1	bL21	
uL22m	MRPL22	W	210	45-210	AK392578.1	uL22	
uL23m	MRPL23	X	150	2-116, 132-150	AK392218.1	uL23	
uL24m	MRPL24	Y	216	13-216	NP_001231376.1	uL24	
bL27m	MRPL27	0	148	35-148	XP_003131628.3	bL27	
bL28m	MRPL28	1	256	2-245	XP_003124744.1	bL28	
uL29m	MRPL47	2	252	66-243	XP_003132595.1	uL29	
uL30m	MRPL30	3	161	35-152	XP_003354768.1	uL30	
bL31m	MRPL55	4	126	35-79	XP_005661204.1	bL31	
bL32m	MRPL32	5	188	79-188, Zn 500	AK343710.1	bL32	Zn ²⁺ binding
bL33m	MRPL33	6	65	13-60	XP_003125332.1	bL33	
bL34m	MRPL34	7	95	50-95	AW415886.1	bL34	
bL35m	MRPL35	8	188	94-188	XP_003124984.1	bL35	
bL36m	MRPL36	9	100	63-100, Zn 500	AK392116.1	bL36	Zn ²⁺ binding
mL37	MRPL37	a	423	30-422	AK237653.1	restriction endonuclease-like	homology to and dimerization with mL65
mL38	MRPL38	b	380	27-380	XP_003131236.1	PEBP-like [§]	
mL39	MRPL39	c	334	30-324	XP_003132793.4	tRNA synthetase domain like [§]	
mL40	MRPL40	d	206	83-181	NP_001230488.1	yeast mL40	extended structure
mL41	MRPL41	e	135	15-135	AW787117.1	yeast mL41	extended structure
mL42	MRPL42	f	142	35-142	AY609966.1	novel fold	extended structure, residues 77-100 built as UNK [‡]

Table S4 (continued).

Protein/ RNA	Old name*	Chain ID	Full size† (residues)	Modeled residues	Sequence accession code	Structural homologs‡	Comments
mL43	MRPL43	g	159	2-149	XP_003483589.1	thioredoxin like§	
mL44	MRPL44	h	332	31-319	NP_001230334.1	RNase III domain-like§	
mL45	MRPL45	i	312	56-297	AK232067.1	cystatin-like§	
mL46	MRPL46	j	279	43-104, 116- 217, 227-279	XP_003121908.1	nudix hydrolase§	
mL48	MRPL48	k	212	48-66, 77-193	AK391730.1	ferredoxin- like§	
mL49	MRPL49	l	166	34-166	NP_001231942.1	eIF1-like§	
mL50	MRPL50	m	159	51-159	XP_003122091.1	ACP-like§	
mL51	MRPL51	n	128	32-128	EW306587.2	STAR protein dimerization domain	2-helical motif surrounded by rRNA
mL52	MRPL52	o	124	23-116	NP_001172080.1	novel fold	extended structure
mL53	MRPL53	p	112	2-98	XP_003125037.1	thioredoxin-like§	
mL54	MRPL54	q	138	102-138	XP_003123104.1	not determined	only C-terminal helix visible
-	MRPL56	-	556	-	NP_001230291.1		not detected
mL62	MRPL58 (ICT1)	u	205	38-85, 93-195	NP_001231224.1	peptidyl-tRNA hydrolase§	residues 164-173 built as UNK‡
mL63	MRPL57 (MRP63)	t	102	9-102	AK347505.1	homeo-domain-like§	
mL64	MRPL59 (CRIF1)	v	222	25-155	XP_003123387.1	novel fold	extended structure, residues 144-155 built as UNK‡
mL65	MRPS30	w	433	40-426	AK236026.1	restriction endonuclease-like	homology to and dimerization with mL37
mL66	MRPS18A	x	196	35-196, Zn 500	FD604770.1	bS18	Zn ²⁺ binding together with uL10
		z		9-36, 99- 106, 300-315, 399-425, 601-615		-	unassigned secondary structure elements, built as UNK‡
16S rRNA		A	1569	1-18, 25-140, 146-886, 889-906, 909-1089, 1122-1211, 1220-1569	AJ002189.1		
CP tRNA		B	73	5-15, 23-53, 58-66			mitochondrial tRNA replacing the 5S rRNA, bases deposited as purines and pyrimidines

* Nomenclature according to the ribosomal protein gene database (65).

† Full-length protein sequences including putative mitochondrial targeting peptides.

‡ Unassigned residues were modeled as poly-serine and deposited as UNK.

§ Fold predicted by the Phyre2 protein fold recognition server (66).

|| PDBeFold search results (67).

Table S5.

Intersubunit bridges in the mammalian mitoribosome. Bridge: bridge name; type: macromolecules involved (R, RNA; P, Protein); 28S/39S subunit component: rRNA and protein residues forming the bridge.

Bridge	Type	28S subunit component	39S subunit component	Comments
B1a	R-P	12S h42: 756-757	Unassigned α -helix	
B1b	R/P-P	12S h42: 756, 771-774 mS29: 169, 276-277 12S: 745-746	mL48: loop 138-144 mL48: β -strand 146-147	
B1c	P-P	mS29: 211-212, 233	mL46: 118-119, 121-122	
B1d	P-P	mS29: 213*, loop 230	mL46: 98*, 101*, 102	
B2a	R-R	12S:430-431 12S: 943 12S h44: 850-853, 920-922	16S H69: 906-915	
B2b*	R-R	12S h24: 423-425	16S: 921-922 16S H68: 877-878	
B2c	R/P-R	mS38: 151, 155, C-terminus (198-199) 12S h27: 504-505	16S H68:871-874	
B2d	P-R	mS38: 159, 163, 193	16S: 968-971	
B2e	R-P/R	12S h24: 412, 415 12S h24: 411-412*	uL2m: 232, 255 16S*: 843-844 (H66), 871-873 (H67), 875 (H67)	possible RNA-RNA interaction mediated by Mg^{2+}
B2f	P-R	mS38: 149, 152	16S H70: 925-927	
B3	R/P-R	12S h44: 909-912 mS38: 156	16S H71: 940-941, 952-955	
B5	R-R/P	12S h44: 862-867	16S H71: 941-943, 951-952 uL14m: loop 49-52, 78	
B6*	R-P	12S h44: 895	bL19m: loop 194-196, 223	
B7a	R-R	12S h23: 353-354	16S: 888-890	Tip of H68 poorly ordered and not built in atomic model, but contact exists based on features of the density.
B7c	P-P	bS6m: 24*, 55, loop 84-86	uL2m: loop 172-176, 220	
B8*	R-P	12S h13: 167-168	uL14m: 43, loop 118, 120	
B9	P-P	mS27: PPR fold	bL19m: N-terminal tail	bL19m and mS27 sequence unassigned

* Contact distance of bridge between 4 Å and 6 Å. Areas of low local resolution or possible presence of poorly ordered ligands that are not built in the atomic model (e.g. Mg^{2+}).

Table S6.

tRNA interactions in the mammalian mitoribosome. List of interactions of the A-site and P-site tRNAs with the 55S mitoribosome. Because of the weak density for parts of the tRNAs and the involvement of protein segments to which no sequence could be assigned in some interactions, additional interactions that have not yet been identified may exist.

Interaction [*]	Type	Ribosomal component	tRNA region [†]	Comments
28S subunit A-site				
a _A	R	12S: 256	Anticodon/anticodon loop	
b _A	R	12S: 614	Anticodon loop	Base of U614 stacked on anticodon; backbone phosphates U612 and A613 coordinate a hydrated Mg ²⁺ ion that stabilizes the A-site tRNA
d _A	R	12S: 918-919	Anticodon	Decoding center bases monitoring base pairing to mRNA
39S subunit A-site				
l _A	P	uL16m: 52, 106	T-loop	
l _A	P	uL16m: 55	T-stem	
	P	P-site finger [‡]	D-stem	
f _A	R	16S H69	D-stem	Residues 907-908 not built but likely involved in contacts to D-stem/D-stem junction
i _A	R	16S: 935	Acceptor stem	
j _A	R	16S: 1273	CCA-3'-end	
h _A	R	16S: 1303	T-stem	
	R	16S: 1315	CCA-3'-end	Bridged by Mg ²⁺ ion
	R	16S: 1327-1328	CCA-3'-end	
k _A	R	16S: 1374-1376	CCA-3'-end	
	R	16S: 1394	CCA-3'-end	
	R	16S: 1404-1406	CCA-3'-end	
28S subunit P-site				
d _P	P	uS9m: 396-397	Anticodon loop	
a _P	R	12S: 713-714	Anticodon loop	
b _P	R	12S: 782-785	Anticodon stem	
c _P	R	12S: 430	Anticodon stem	
d _P	R	12S: 571	Anticodon loop	Interacts with backbone of anticodon
f _P	R	12S: 844	Anticodon	Stacks onto anticodon base
39S subunit P-site				
	P	bL27m: 35, 36, 38	Anticodon stem	N-terminus of bL27m not built; additional contacts closer to the tRNA 3'-end likely
	P	P-site finger [‡]	D-stem junction/D-stem	Additional interactions with T-stem likely
g _P	R	16S H69: 901-903, 915-917	Anticodon stem, D-stem	
	R	16S: 1056-1057	CCA-3'-end	
i _P , j _P	R	16S: 1149-1151, 1153	Acceptor stem, CCA-3'-end	
	R	16S: 1260	CCA-3'-end	
	R	16S: 1271-1272	CCA-3'-end	
l _P	R	16S: 1406	CCA-3'-end	
k _P	R	16S: 1422-1424	CCA-3'-end	

^{*} Interactions conserved between mitochondrial and bacterial ribosomes are denoted according to the nomenclature in (17).

[†] Due to the mixture of tRNAs bound to the 55S mitoribosome in our sample, the identity of individual tRNA nucleotides cannot be established

[‡] Sequence unassigned

Table S7.

Mass-spectrometric identification of mS38 peptides. Two mass-spectrometric experiments were conducted after digestion of 55S mitoribosomal sample with trypsin. Identified fragments, Mascot score, Expect value, and peptide sequence are given. Peptides that were identified with low reliability (Mascot score below 20) are indicated in red.

Residues	Mascot Score	Expect	Peptide
<i>Experiment 1</i>			
129-134	14	0.036	K.NILKIR.R
180-193	76	2.6×10^{-8}	K.AGLKEAPAGWQTPK.I
180-193	60	1×10^{-6}	K.AGLKEAPAGWQTPK.I
180-193	49	1.2×10^{-5}	K.AGLKEAPAGWQTPK.I
180-193	53	5.6×10^{-6}	K.AGLKEAPAGWQTPK.I
184-193	44	4×10^{-5}	K.EAPAGWQTPK.I
184-193	35	0.0003	K.EAPAGWQTPK.I
184-193	48	1.5×10^{-5}	K.EAPAGWQTPK.I
<i>Experiment 2</i>			
180-193	25	0.0032	K.AGLKEAPAGWQTPK.I
180-193	61	7.4×10^{-7}	K.AGLKEAPAGWQTPK.I
180-193	63	5.5×10^{-7}	K.AGLKEAPAGWQTPK.I
180-193	41	7.4×10^{-5}	K.AGLKEAPAGWQTPK.I
180-193	39	0.00012	K.AGLKEAPAGWQTPK.I
184-193	52	6.1×10^{-6}	K.EAPAGWQTPK.I
184-193	53	5.4×10^{-6}	K.EAPAGWQTPK.I
184-193	30	0.001	K.EAPAGWQTPK.I
194-199	18	0.017	K.IYLKNQ.-

Additional Data Table S1 (separate file)

Overview of 55S mitoribosomal proteins and isoforms identified by mass spectrometry.

References

41. X. Li *et al.*, Electron counting and beam-induced motion correction enable near-atomic-resolution single-particle cryo-EM. *Nat. Meth.* **10**, 584-590 (2013).
42. S. J. Ludtke, P. R. Baldwin, W. Chiu, EMAN: semiautomated software for high-resolution single-particle reconstructions. *J. Struct. Biol.* **128**, 82-97 (1999).
43. J. A. Mindell, N. Grigorieff, Accurate determination of local defocus and specimen tilt in electron microscopy. *J. Struct. Biol.* **142**, 334-347 (2003).
44. S. H. W. Scheres, RELION: Implementation of a Bayesian approach to cryo-EM structure determination. *J. Struct. Biol.* **180**, 519-530 (2012).
45. M. Heublein *et al.*, The novel component Kgd4 recruits the E3 subunit to the mitochondrial α -ketoglutarate dehydrogenase. *Mol. Biol. Cell*, (2014).
46. T. A. Jones, J. Y. Zou, S. W. Cowan, M. Kjeldgaard, Improved methods for building protein models in electron density maps and the location of errors in these models. *Acta Crystallogr. A Found. Crystallogr.* **47 (Pt 2)**, 110-119 (1991).
47. T. A. Jones, Interactive electron-density map interpretation: from INTER to O. *Acta Crystallogr. D Biol. Crystallogr.* **60**, 2115-2125 (2004).
48. P. Emsley, B. Lohkamp, W. G. Scott, K. Cowtan, Features and development of Coot. *Acta Crystallogr. D Biol. Crystallogr.* **66**, 486-501 (2010).
49. P. D. Adams *et al.*, PHENIX: a comprehensive Python-based system for macromolecular structure solution. *Acta Crystallogr. D Biol. Crystallogr.* **66**, 213-221 (2010).
50. P. V. Afonine *et al.*, Towards automated crystallographic structure refinement with phenix.refine. *Acta Crystallogr D Biol Crystallogr* **68**, 352-367 (2012).
51. L. Urzhumtseva, P. V. Afonine, P. D. Adams, Crystallographic model quality at a glance. *Acta Crystallographica ...*, (2009).
52. B. S. Schuwirth *et al.*, Structures of the bacterial ribosome at 3.5 Å resolution. *Science* **310**, 827-834 (2005).
53. E. Krissinel, K. Henrick, Inference of macromolecular assemblies from crystalline state. *J. Mol. Biol.* **372**, 774-797 (2007).
54. E. F. Pettersen *et al.*, UCSF Chimera--a visualization system for exploratory research and analysis. *J. Comput. Chem.* **25**, 1605-1612 (2004).
55. A. Kucukelbir, F. J. Sigworth, H. D. Tagare, Quantifying the local resolution of cryo-EM density maps. *Nat. Meth.* **11**, 63-65 (2014).
56. J. A. Dunkle *et al.*, Structures of the bacterial ribosome in classical and hybrid states of tRNA binding. *Science* **332**, 981-984 (2011).
57. A. Ben-Shem *et al.*, The structure of the eukaryotic ribosome at 3.0 Å resolution. *Science* **334**, 1524-1529 (2011).
58. S. H. W. Scheres, S. Chen, Prevention of overfitting in cryo-EM structure determination. *Nat. Meth.* **9**, 853-854 (2012).
59. P. B. Rosenthal, R. Henderson, Optimal determination of particle orientation, absolute hand, and contrast loss in single-particle electron cryomicroscopy. *J. of Mol. Biol.* **333**, 721-745 (2003).
60. J. Frank, R. K. Agrawal, A ratchet-like inter-subunit reorganization of the ribosome during translocation. *Nature* **406**, 318-322 (2000).

61. X. Agirrezabala *et al.*, Visualization of the hybrid state of tRNA binding promoted by spontaneous ratcheting of the ribosome. *Molecular Cell* **32**, 190-197 (2008).
62. T. V. Budkevich *et al.*, Regulation of the mammalian elongation cycle by subunit rolling: a eukaryotic-specific ribosome rearrangement. *Cell* **158**, 121-131 (2014).
63. O. T. Fischmann *et al.*, Structural characterization of nitric oxide synthase isoforms reveals striking active-site conservation. *Nat. Struct. Biol.* **6**, 233-242 (1999).
64. N. Ban *et al.*, A new system for naming ribosomal proteins. *Current Opinion in Structural Biology* **24**, 165-169 (2014).
65. A. Nakao, M. Yoshihama, N. Kenmochi, RPG: the Ribosomal Protein Gene database. *Nucleic Acids Research* **32**, D168-170 (2004).
66. L. A. Kelley, M. J. E. Sternberg, in *Nat Protoc.* (2009), vol. 4, pp. 363-371.
67. E. Krissinel, K. Henrick, Secondary-structure matching (SSM), a new tool for fast protein structure alignment in three dimensions. *Acta Crystallogr. D Biol. Crystallogr.* **60**, 2256-2268 (2004).